Structural mapping of patient-associated *KCNMA1* gene variants

Hans J. Moldenhauer[1], Kelly Tammen, and Andrea L. Meredith[1*]

[1]Dept. of Physiology, University of Maryland School of Medicine, Baltimore, MD, USA

[*]Corresponding author: Andrea L. Meredith

Dept. of Physiology

University of Maryland School of Medicine

655 W. Baltimore St.

Baltimore, MD 21201

Tel: (410) 706-5991

Fax: (410) 706-8341

ameredith@som.umaryland.edu

Running title: *KCNMA1* variants in the BK channel

Key words: BK channel, KCa1.1, calcium-activated potassium channel, *KCNMA1*, potassium channel, Slo1, slowpoke, channelopathy, pathogenicity algorithm

Article type: Research article

Main Figures: 8

Supplemental Figures: 2

Supplemental Tables: 2

Abstract

KCNMA1-linked channelopathy is a neurological disorder produced by malfunctioning of the BK channel, characterized by seizure, motor abnormalities, and neurodevelopmental disability. Twenty-one *KCNMA1* patient-associated variants have been classified as gain-of-function (GOF) or loss-of-function (LOF) in BK channel activity, and the remaining ~40% are variants of uncertain significance (VUS). To address the physical relationships, this study analyzed *KCNMA1* missense variants within the context of BK channel cryoEM structures. Clusters of LOF variants were identified in the pore, within the AC region (RCK1), and near the Ca^{2+} bowl (RCK2), overlapping with sites of pharmacological or endogenous modulation. However, no clustering relationship was found for GOF variants. Next, variants were analyzed with widely used pathogenicity algorithms. The individual performances of REVEL, Mutpred, MetaLR, and CADD/PHRED were compared for each variant, incorporating them into a weighted summation model (WSM). The WSM component was integrated with BK channel structural parameters in a modular algorithm to generate a 'KCNMA1 meta score' (KMS). KMS performance showed a 7% difference from the highest performing individual algorithm (REVEL). Several functionally uncharacterized variants that showed different predictions between KMS and REVEL were assessed further using electrophysiological recordings of BK currents. Two KMS^{+}; $REVEL^{-}$ variants were confirmed pathogenic (M578T and D965V), and one KMS^{-}; $REVEL^{+}$ variant was confirmed non-pathogenic (D800Y). However, KMS failed to accurately categorize two variants (E656A and K457E). Thus, although incorporation of structural data within the KMS algorithm results in a small performance improvement, its predictive capabilities will be increased as more disease-delineated variants are functionally tested, new structural components are available, and novel functional modules are developed.

Introduction

KCNMA1-linked channelopathy is a rare, predominantly neurological syndrome of incompletely defined phenotypes associated with mutations in the *KCNMA1* gene (Meredith 2024). The protein product of the *KCNMA1* gene is the pore-forming subunit of the calcium and voltage-activated BK K^+ channel (Dworetzky et al 1994, McKay et al 1994, Pallanck & Ganetzky 1994). BK channels regulate neuronal, muscle, and neuroendocrine cell excitability, with additional roles in non-excitable cells in tissues such as kidney, bone, and gastrointestinal tract (Brenner et al 2000, Dworetzky et al 1994, McCobb et al 1995, Uhlen et al 2015). Overlapping symptomology between patients has identified four main dysfunctions in individuals with *KCNMA1* variants: epilepsy, movement disorder, neurodevelopmental delay and intellectual disability, and structural malformations (Bailey et al 2019, Miller et al 2021). However, there is high phenotypic variability. Moreover, it is currently unclear whether all *KCNMA1* variants discovered through genetic testing are causative, or whether identified variants contribute to a more complex disease etiology through interactions with other genes.

At present, two variants (D434G and N999S) are conclusively determined to cause neurological disease, based on co-segregation of seizure and paroxysmal nonkinesigenic dyskinesia (PNKD) in a family pedigree and recapitulation of those phenotypes in animal models (Dong et al 2021, Du et al 2005, Kratschmer et al 2021, Park et al 2022). Another variant tested (H444Q) appears to require additional genetic or other factors for pathogenicity in mice (H444Q)(Park et al 2022). In addition, statistical correlation in unrelated patients associates *de novo* GOF variants with PNKD and *de novo* LOF variants with other types of movement disorder, neurodevelopmental diagnoses, and structural malformations in 2021 (Miller et al 2021). These phenotypic similarities among GOF variants within *KCNMA1*-

linked channelopathy, and the GOF versus LOF variant differences, are derived from 75 patient-associated variants included in this study. However, the variant phenotypes are not understood with respect to BK channel structure and function.

The goal of this study was to localize and visualize *KCNMA1* variants within the tetrameric BK channel pore-forming subunit. In the first step, we undertook a comprehensive annotation of the cryoEM structure to probe the functional and domain-based associations for patient-associated variants. In the second step, we integrated structural information into an ensemble algorithm (*KCNMA1* Meta Score) and identified several variants where this structural integration differed from the pathogenicity prediction obtained with standard genetic algorithms such as REVEL. These variants were assessed for functional effects on BK channel properties using patch-clamp electrophysiology in heterologous cells.

Methods

Linear Sequence Annotation

KCNMA1 variants were annotated in the human BK channel sequence MG279689 (Supplemental Figure 1). This isoform has the alternative exons SRKR (site 1), no insert (site 2; STREX), Ca^{2+} bowl (site 3), and VYR (site 4; C-term). Variants were obtained from ClinVar, the Sanford Coordination of Rare Diseases (CoRDs) Registry, and direct submissions under University of Maryland School of Medicine IRB Non-Human Subject Research (NHSR) designations HP-00083221 and HP-00086440. Single nucleotide polymorphisms (SNPs) were obtained from gnomAD.

Structural and cluster analysis

Clustering of residues was evaluated in Visual Molecular Dynamics (VMD, University of Illinois). The cluster analysis for patient variants and SNPs consists of

calculating the proximity of three residues at 5Å between alpha carbon's distance within the domain (Supplemental Table 2). This distance is considered the average interaction distance in energetic terms (Samudrala & Moult 1998). For reference, the gating ring measures 43.5 Å across in the open state between K384 α carbons of diagonal subunits, and the channel's length is 105.6 Å between Q19 in the N terminal and M712 in the RCK2. Residue pairs were defined with these same parameters, but only between two residues. The analysis was performed on the cryo-EM BK channel Ca^{2+} open channel structure (PDB ID:6V38) and cryo-EM BK channel Ca^{2+} free closed channel structure (PDB ID: 6V3G) (Tao et al. 2017). Since no change in classifications of pairs and clusters were observed, the calcium bound channel was utilized for representation in each figure. This cryo-EM structure spans amino acid 19 to 1056 and lacks the regions between the amino acids: 51 to 93, 613 to 684, and 833 to 871 (Supplemental Figure 1). The VMD visualization settings were 'cartoon' for the complete channel structure and 'Van der Waals (VDW)' for representation of individual residues of interest. Additionally, four patient variants corresponding to channel truncations were generated within the cryo-EM structure (PDB ID:6V38) (Tao et al 2017) and compared with two experimentally truncated channels: Slo1C truncates in the linker between S6 and RCK1 at position 342 and Slo1ΔRCK2 truncates after RCK1 at position 632 (Budelli et al 2013). The Slo1C representation does not include the 74 amino acid tail, or the 11 amino acid residues from Kv1.4, that were included in the published Slo1C construct. The Slo1ΔRCK2 structural model was used as reference for the RCK1 and RCK2 boundaries for comparison to other representation truncation variants. Nonsynonymous single nucleotide polymorphisms (SNPs) from GenomAD (ENSG00000156113.16), Plante et al. 2019 and Miller et al., 2021 were added onto the cryo-EM structure (PDB ID: 6V38).

Pharmacological and Intracellular Modulators

Thirteen of sixteen modulators (agonist, antagonist, and endogenous molecules) with action on the alpha subunit of the BK channel were mapped. The agonists included were BC5 (Guohui Zhang et al., 2022), NS1619 (Gessner et al., 2012), NS11201 (Rockman et al., 2020) and Cym04 (Gessner et al., 2012). The antagonists were charybdotoxin (ChTX) (Qiu et al., 2009), iberiotoxin (IbTX) (Yu et al., 2016), loperamide (LOP) (Vouga et al., 2019), paxilline (PAX) (Zhou et al., 2020), and TEA (Crouzy et al., 2001; Lenaeus et al., 2005). The endogenous modulators were Heme (Tang et al., 2003), protons (H^+) (Hou et al., 2009), lipids (Xia et al., 2004), carbon monoxide (CO) (Hou et al., 2008), kinases (Yan et al., 2008) and ethanol (EtOH) (Bukiya et al., 2014). Phospho-sites are numbered in the context of the BK channel cDNA NM_001161352.2. Only modulators with confirmed or putative binding sites were included.

Pathogenicity scores

The algorithms SIFT, Polyphen, CADD/PHRED, MetaLR, M-CAP, Mutpred and REVEL were evaluated in their predictor value for the *KCNMA1* patient mutations using the online variant predictor tool from www.ensembl.org. Default settings were used with the *KCNMA1* reference sequence number associated with the human patient variants reported in Clinvar database: NM_001161352.2. The parameters evaluated were accuracy (how close the pathogenic scores are from confirmed ones), precision (how close the pathogenic variant scores are), specificity (ability to detect a benign variant correctly), and sensitivity (ability to identify a pathogenic variant correctly) according to the equations 1 to 4 using the pathogenicity scores obtained for the confirmed benign and pathogenic variants (Figure 6A and Supplemental Table 1):

1. $Sensitivity = \frac{TP}{(TP+FN)}$

2. $Specificity = \frac{TN}{(TN+FP)}$

3. $Precision = \frac{TP}{(TP+FP)}$

4. $Accuracy = 2 * \frac{Precision*Sensitivity}{(Presicion+Sensitivity)}$

With the abbreviations of TP being true positive, TN being true negative, FP being false positive and FN being false negative. The numbers associated to each term vary between algorithms and are based on the confirmed pathogenic and non-pathogenic variants (Figure 7A, green nonpathogenic and red pathogenic). The total performance score for each algorithm was calculated averaging the 4 parameters to determine the goodness series to determine its inclusion in the *KCNMA1* meta score algorithm construction (Supplemental Figure 2) (Ganakammal & Alexov 2019).

***KCNMA1* meta score (KMS) algorithm**

To construct the KMS algorithm, we use a weighted summation model (WSM) that incorporated structural information (Ganakammal & Alexov 2019, Holland et al 2017) from REVEL, Mutpred, MetaLR and CADD/PHRED. Since the 3 of the 4 algorithms ranged from 0 to 1, the range for CADD/Phred was adjusted to avoid over-representation in the WSM. Then a structural component (SC) was calculated from the human *KCNMA1* cryo-EM structures in absence and presence of Ca^{2+} (PDB:6V3G and 6V38) (Hite et al 2017b, Tao et al 2017) using the 5Å criteria explained in the cluster analysis. The SC consist in the interactions and the energy associated between residues, calculated using the web based algorithm RING with the default settings (https://ring.biocomputingup.it/submit) (Clementel et al 2022) to determine the number of interactions (NI) and average energy (AE), and the

number of residues (NR) using the ProteinTools web tool (https://proteintools.uni-bayreuth.de) (Ferruz et al 2021) (Supplemental Table 2).

Cut-off determinations

The cut-off determination for significance for KMS and the seven pathogenicity algorithms was made using the logistic regression method. Data dichotomization was performed, assigning a value of 1 to the 22 pathogenic variants: A172T, A314T, S351Y, G354S, G356S, G375R, C413Y, D434G, H444Q, N449fs, K457E, R458Ter, N536H, G567S, I663V, E736K, P805L, E884K, D984N, N999S, R1083K, R1097H and 0 to benign variants: K518N, E884K, R1128W and N1159S, as confirmed by experimental and/or genetic data. Then, pathogenicity scores for the four best performing algorithms (REVEL, CADD/Phred, Mutpred2 and MetaLR) were plotted against its assigned dichotomic values. A logistic regression fit was applied, and a receiver operating characteristic (ROC) curve generated using the software Prism 9 (GraphPad Software, San Diego, California USA). From the ROC curves the best cut-off was determined based on the point resulting in the lowest false positive and the highest true positive values based on known pathogenic/non-pathogenic variants (Supplemental Figure 2).

Synthesis of *KCNMA1* patient variants in the human BK channel

The variants D800Y, D965V, E656A and M578T were introduced by site-directed mutagenesis in a wildtype (WT) human BK channel in pcDNA3.1+ (Bioinnovatise, Rockville, MD) and verified by sequencing). The BK channel cDNA includes Myc at the N-terminus and the EYFG tag inserted at exon 22, at position 716 in RCK2 (Plante et al 2019). YFP fluorescence was used to identify transfected cells. These tags do not affect BK current properties (Giraldez et al 2005, Plante et al 2019).

Electrophysiology

HEK293T cells were used to express the BK channel constructs (CRL-11268, ATCC, Manassas, VA, USA). The cell culture was incubated at 37°C with 5% carbon dioxide. The cells were plated on 35 mm tissue culture dish and fed with DMEM containing media (Cat. #11995-065, Gibco, Life Technologies Corp., Grand Island, NY, USA) supplemented with: 10% fetal bovine serum (Cat. #4135, Sigma-Aldrich, St. Louis, MO, USA), 1% penicillin/streptomycin (Cat. #30-002-Cl, Mediatech Inc., Manassas, VA, USA) and 1% L-glutamine (Cat. #25-005-Cl, Mediatech Inc., Manassas, VA, USA). Cells were transfected at 60-70% confluency using Trans-IT LT1 (Mirius Biological, Madison, WI, USA) at 1:2 ratio of cDNA to transfection reagent (μg/μL). After 6 hours, cells were re-plated onto poly-L-lysine glass coverslips (Cat. #P4832, Sigma-Aldrich, St. Louis, MO, USA). The recordings were performed at 14-24 hours post-transfection.

Electrophysiology solutions approximated the physiological K^+ gradient with 10 μM intracellular free Ca^{2+}. The external (pipette) solution contained (in mM): 134 NaCl, 6 KCl, 1 $MgCl_2$, 10 glucose, and 10 HEPES with pH adjusted to 7.4 with NaOH. The internal (bath) solution contained in mM: 110 $KMeSO_3$, 10 NaCl, 30 KCl, 10 HEPES, 1 $MgCl_2$, 5 HEDTA and 10 μM $CaCl_2$. The pH was adjusted to 7.2 with KOH. The desired nominal Ca^{2+} concentration was achieved using WebMaxC to calculate the volume of a 1 M $CaCl_2$ stock (Thermo fisher) in HEDTA (http://web.stanford.edu/~cpatton/webmaxcS.htm).

Macroscopic currents were recorded in inside-out patch clamp configuration at room temperature (22°C to 24°C). Electrodes were made from thin-walled borosilicate glass pipettes, with resistances of 2-3.5 MΩ (Cat. #TW150F-4, World Precision Instruments, Sarasota, FL, USA). Voltage commands were applied with a MultiClamp 700B amplifier

(Axon Instruments, Sunnyvale, CA, USA) through a Digidata 1440/1550B interface with CLAMPEX 10/11 suite (Molecular devices). Three current traces were acquired at 50 kHz, filtered online at 10 kHz, and averaged offline. Two voltage step protocols were used for activation and deactivation, respectively. The activation protocol stepped from a V_{hold} of −150 mV to +150 mV (Δ+10 mV increments) for 50 ms and back to −150 mV for 15 ms to generate tail currents. Conductance (G) was calculated from tail currents, 150-200 µs after the peak, and normalized to the highest conductance calculated for each patch (G/G_{max}). G/G_{max} values were plotted against membrane potential (V) to generate conductance-voltage (G/G_{max}-V) curves. The voltage of half maximal activation ($V_{1/2}$) values were calculated by fitting the G/G_{max}-V relationship to a Boltzmann function using Prism v9, constrained to 1 at top and 0 at bottom (GraphPad Software, San Diego, California USA). The deactivation time constant (τ_{deact}) were obtained from BK currents activated by 20 ms voltage steps of +200 mV from a V_{hold} of -150 mV, followed by 15 ms voltage steps from -200 mV to -50 mV (Δ+10 mV increments). Activation time constants (τ_{act}) were obtained from the voltage activation protocol, by fitting a single standard exponential to the rising phase of the current. Deactivation kinetics were measured by fitting the tail current decay with a single exponential function in pCLAMP 10.6 (Molecular Devices, San Jose, CA, USA). In all protocols, leak current was subtracted using a P/5 protocol with a subsweep V_{hold} of -120 mV.

Statistics

BK current analysis was performed with pClamp 10.6 (Molecular Devices, San Jose, CA, USA). Graphs and statistical analysis were generated in Prism v9 (GraphPad Software, San Diego, CA, USA). Two-way ANOVA with Bonferroni post-hoc tests were used to determine significance for $V_{1/2}$ and activation/deactivation kinetics at $p < 0.05$.

Results

Locations and clustering of LOF and GOF *KCNMA1* variants

To date, 75 nonsynonymous *KCNMA1* human patient (HP) associated variants have been reported in 106 individuals with heterogeneous neurological symptoms (Bailey et al 2019, Meredith 2024, Miller et al 2021)(and ALM unpublished data). Nine variants were located within unresolved regions in the cryoEM structure or occurred in alternate exons and were not analyzed. Thirteen of these variants produced deletions or frameshifts. To understand the structural relationships for variants altering single amino acids with the BK channel, 53 variants were mapped onto the human Ca^{2+} bound BK channel cryo-EM structure and assessed with respect to the Ca^{2+} binding sites, Mg^{2+} binding site, voltage sensor and selectivity filter residues, pharmacological modulator binding sites, and post translational modifications (Figure 1 and Supplemental Figure 1). Of these 53 variants, 15 were categorized as loss of function (LOF), 3 as gain of function (GOF), and 4 as benign from functional studies of BK currents and/or expression. Of the 31 variants of uncertain significance (VUS) that have not yet been studied functionally, 9 are currently predicted pathogenic by ClinVar.

The first observation identifies HP variants in the three main channel modules: pore domain (PD), voltage sensing domain (VSD) and the gating ring (Figure 1A and B). Interestingly, only 10 HP variants were in the transmembrane segments (Figure 1C top view) compared to the 43 located in the intracellular part of the channel (the intracellular linkers and gating ring) (Figure 1D bottom view). HP variants A172T, T176S, L226F, N237K, L271F and A314Y located in the VSD are at distances above 5Å from the residues involved in the voltage activation R178, D198, D218, R232, E245, D251, R272, R275, R278 and E284

(Carrasquel-Ursulaez et al 2022). The only exceptions were A172 and T176S (3.3 and 3.2Å from R178 in S1) and L271F (4.8Å from R275 in S4).

Next, we determined the clustering of HP variants by localizing the confirmed LOF and GOF HP mutations in the BK channel structure (Figure 2A). A cluster was defined as three residues within 5Å in a domain. In the case of the LOF variants, fifteen of twenty-one variants were placed onto the BK channel cryo-EM structure. Four terminations R458Ter, R640Ter, R830Ter, R880Ter, and the two frameshift N449fs and Y676fs, were excluded since the electrophysiological phenotypes may be due to the sequence truncation or alteration and not to mutation residue itself. In a detailed examination of the LOF variants, two clusters and two pairs were observed. Only three of the fifteen LOF variants, A172T, N237K, and R1097H, did not fall within a pair or cluster (Figure 2A). One of the clusters of LOF variants occurs within the PD (Figure 2A and B). The cluster includes the variants A314Y, S351Y, G354S, G356R and G375R. This PD cluster spans 20.3 Å, including residues from the transmembrane region S5, selectivity filter (SF), and the transmembrane region S6 that forms the inner vestibule. Inside the PD cluster, there is a sub-cluster in the SF between S351, G354, and G356 with distances of 5.85 Å between S351 and G354 and 3.66 Å between G354 and G356. The G354 and G356 residues are part of the well characterized 'GYG' signature sequence that confer the high K^+ selectivity (Doyle et al 1998).

The second cluster of LOF variants occurs in the βA-αC (AC) region of the RCK1 domain (Yang et al 2010) including the variants C413Y, H444Q, and K457E (Figure 2A and D). The variants R458ter and N449fs also fall in this subdomain but were not considered a part of the cluster as detailed above. The AC region cluster spans 22.6 Å, with variants C413Y and H444Q separated at 5.9 Å and H444Q and K457 separated by 14.7 Å. The relevance of the αβ helix of the AC region has been demonstrated in the past by mutagenesis,

showing changes in the $V_{1/2}$ when it is modified (Niu et al 2004), similar to the phenotypes produced by LOF variants in this region (Geng et al 2020). Interestingly, D434G, a well-characterized GOF mutation located in the AC region that produces increased channel activity, could be considered part of this cluster in terms of distance but not in terms of its GOF phenotype (Moldenhauer 2019, Wang et al 2009b, Yang et al 2010).

A pair of LOF variants, D965V and D984N, occur in a highly conserved subdomain of RCK2 containing a calcium binding site (Figure 2A) (Schreiber & Salkoff 1997, Tao et al 2017). D965V and D984N reside within 5 Å of the calcium bowl (3.4 Å and 4.5 Å, respectively), with a distance of 14.5 and 14.7 Å to the Ca^{2+} ion (Figure 2D). Another pair of LOF variants, R800W and P805L, also occur in RCK2. These residues are located 4.9 Å apart, at the end of S9 and in the S9-S10 linker (Figure 2A and D). While not considered a part of a cluster or pair, R1097H occurs close to the R800W/P805L pair, separated from the other two residues by 7.8 Å. This distance was not considered for the purpose of determining clustering here since the cut-off was 5 Å. However, values greater than 5 Å have been used in other clustering determination studies (Maljkovic 2019, Pape et al 2010). Thus, the clustering of LOF HP variants showed a relationship between the structural location and the biophysical properties associated with the amino acid change.

The three GOF variants, D434G, N536H, and N999S, do not share an observable clustering pattern between them, with respect to either function or distance (Figure 2A and C). These variants occur in the gating ring, with D434G and N536H in RCK1 and N999S in RCK2. The D434G residue is located in the AC region but has the opposite electrophysiological phenotype, producing a $V_{1/2}$ shift to negative potentials (Du et al 2005, Moldenhauer et al 2020, Wang et al 2009a, Yang et al 2010), as the LOF variant cluster in the same region (Du et al 2020, Li et al 2018b, Liang et al 2019, Liang et al 2022). Thus,

unlike LOF variants, no cluster for GOF HP variants was observed under the criteria of occurring within a structural domain or 5 Å distance. However, D434G and N536H are the closest variants to the Ca^{2+} binding site in the RCK1 with 13 and 15.1 Å respectively. Despite the proximity, D434G and N536H affect the gating properties in different ways, with D434G only affecting the Ca^{2+} activation (Wang et al 2009a, Yang et al 2010, Zhang et al 2020). This is different from N999S, which is 35.2 Å from the Ca^{2+} site, and its effect over the channel gating is not related with Ca^{2+} activation (Li et al 2018b).

Single Nucleotide Polymorphism (SNP) locations

While HP variants suggest deleterious effects on BK channel properties, SNP residues are a potential source of tolerated variability in the gating properties (Miller et al 2021, Plante et al 2019). The *KCNMA1* gene contains 537 non-synonymous SNPs. Of these, just over half (298 SNPs) were located in resolved regions and could be mapped onto the BK channel structure. 142 SNPs were conservative residue changes, based amino acid biochemical properties, and 156 were non-conservative. Figure 3 shows the 298 *KCNMA1* SNPs together with the GOF and LOF HP variants. Overall, there were many conservative SNPs at the N-terminus. Starting from the extracellular side, 52 SNPs occur in the unresolved N-terminus, and 35 of these are NC. Thirty-three SNPs are located in the glycine and serine repeats (Figure 3A, C and Supplemental Figure 1). The intracellular loop between transmembrane segments S0 and S1 contains 38 SNPs, and 26 of these are non-conservative.

The number of SNPs greatly decreases within the core alpha helices and transmembrane segments. The transmembrane segments S3-S6 contain a total of 3 non-conservative SNPs, distributed between S3 and S5 (Figure 3A and B). In the gating ring, 39 SNPs occur after the end of RCK2, which includes 21 that are non-conservative (Figure 3A

and D). Finally, 154 SNPs are not shown due to their locations within unresolved structure regions. Thus, the BK channel N-terminus and gating ring are hot spots for SNP variability, in contrast to the VSD and PD.

Despite the presence of SNPs across the BK channel domains, several regions notably lack non-conservative SNPs. One is the pore (S5 to S6), a region critical for K^+ permeation containing a cluster of LOF HP variants. Another region is the alpha beta helix that interfaces with the voltage-sensing domain in the AC region of RCK1, containing 3 LOF HP variants (Figure 3A). However, the opposite is observed in transmembrane segments S3 and S4, a region containing one non-conservative SNP but lacking HP variants (Figure 2A and 3A). Finally, the calcium bowl lacks SNPs, potentially due to the importance of this motif in the gating of the BK channel (Bao et al 2002, Zhang et al 2010). Taken together, this analysis reveals the domains with decreased non-conservative SNPs and HP variants, hypothesizing lower tolerance to functional changes, compared to domains with an increased number of SNPs.

Sites of pharmacological modulation

BK channel gating properties are regulated by a variety of endogenous intracellular compounds or pharmacological agonists and antagonists. These modulators are relevant as potential therapeutics for *KCNMA1* channelopathy. To determine if HP variants were located near sites of modulation, binding sites and residues involved in modulation sites were localized with respect to HP variants within the BK channel structure. The inhibitors included in this analysis were charybdotoxin (ChTX) (Qiu et al 2009), iberiotoxin (IbTX) (Yu et al 2016), loperamide (LOP) (Vouga et al 2019), paxilline (PAX) (Zhou et al 2020) and TEA (Crouzy et al 2001, Lenaeus et al 2005). The agonists were BC5 (Guohui Zhang1 et al 2022),

NS1619 (Gessner et al 2012), NS11201 (Rockman et al 2020) and Cym04 (Gessner et al 2012). The endogenous modulators were Heme (Tang et al 2003), protons (H^+) (Hou et al 2009), lipids (Xia et al 2004), carbon monoxide (CO) (Hou et al 2008), kinases (Yan et al 2008), and ethanol (EtOH) (Bukiya et al 2014) (Figure 4A and B).

The antagonists LOP, ChTX, IbTX and TEA (external binding site) cluster in the pore domain, acting as blockers in a range of 6.6 in the X axis and 8.3 Å in the Y axis. Interestingly, from the inner vestibule, the agonist NS11201 and antagonists LOP, TEA (internal binding site), and PAX cluster in S6 of the channel with 2.5 and 2.9 Å between residue binding sites (Figure 4A and E). NS11201 shares part of the modulation area with LOP, despite its opposite agonist effect over the BK channel activation. This S6 modulation cluster overlaps with the LOF HP variants S351Y, G354S, G356S and G375R. The ChTX and IbTX binding sites are located in the extracellular loop that connects the pore and S6, composed by site 1 in the selectivity filter and other residues in the turret that stabilize block. No HP variants are currently found in this specific area (Figure 4E).

In the case of the endogenous intracellular modulators, residues involved in EtOH (activator), CO (activator), lipid (activator), and H^+ (activator) modulation cluster at the start of RCK1, at distances of 4.2 and 9.5 Å respectively. Overlapping residues are found between CO, H^+, EtOH, and the LOF variant K457E (Figure 4A and D). Additionally, the sites overlap at 3.8 Å of distance with the BC5 agonist at the start of RCK1.

Marking sites of kinase modulation, 30 residues were detected as phospho-sites by mass spectrometry from rat brain tissue (Yan et al 2008). Only 4 of these residues were located within resolved areas of the structure: S582 (occurring at the end of S7 in RCK1), S850 (between S9 and S10 in RCK2), T1065 (end of RCK2 after S10), and S1123 (after RCK2). No clustering was observed between any of these 4 phospho-sites and HP variants.

However, due to the low number of phospho-sites within resolved regions, no conclusions are currently suggested. Generally, the analysis of modulator and binding sites showed a low number of proximal or overlapping HP mutations. One exception was the pore domain, where the LOF variants and several pharmacological inhibitors have effect over BK channel activity in the same direction.

***KCNMA1* HP variants producing putative truncations**

Four nonsense HP variants are predicted to produce truncated BK channel proteins: R458Ter, R640Ter, R830Ter, and R880Ter (Yesil et al 2018) (ClinVar and ALM unpublished data). Assuming proper folding of the channel with the deleted residues, these putative truncations were schematized to determine the relationships between structural boundaries and BK channel terminations (Figure 5A-D). The representations were then compared with two experimentally truncated channels: Slo1C and Slo1ΔRCK2. Slo1C terminates in the linker between S6 and RCK1 at position 342 and is missing the whole gating ring. Slo1C is characterized as a LOF mutation by electrophysiology, affecting the allosteric interactions in the BK channel gating mechanism (Budelli et al 2013). Slo1ΔRCK2 terminates after RCK1 at position 632. It has not been studied functionally, but clearly delineates the RCK domain boundaries in the gating ring domain.

The R458Ter variant has a LOF phenotype with the putative truncation occurring in the AC region of RCK1 (Figure 5A) (Tabarki et al 2016). The R640Ter variant creates the putative truncation before the alternative splice site 1 in RCK1 (Figure 5B) (Yesil et al 2018). The R830Ter variant creates a putative termination before S9 at the start of RCK2 (Figure 5C). All three are classified as pathogenic by ClinVar. Variant R880Ter is located within RCK2 with the truncation occurring after S9 and before the calcium bowl (Figure 5D) and is

classified as VUS. Only R458Ter has direct electrophysiological evidence for a LOF classification. The three other truncations (R640Ter, R830Ter, and R880Ter) are functionally unstudied at present.

Deletions within the BK channel gating ring could create a LOF BK channel due to loss of the calcium binding sites (Krishnamoorthy et al 2005). The Slo1C truncation occurs at the end of the tetramerization domain after S6 and before RCK1 at position 342 (Figure 5E). Slo1C and R458Ter have a similar termination positioning and result in comparable electrophysiological properties (Budelli et al 2013, Miller et al 2021). However, patients are heterozygous for these variants, and these truncations have the potential to produce more complex BK channel alterations. Truncations could also theoretically produce a GOF effect, if some structural or allosteric restrictions from the gating ring are removed. In the case of R830Ter and R880Ter, which along with SloΔRCK2 have not been characterized electrophysiologically, one Ca^{2+} site is deleted. If functional BK channels are formed these with variants, the final effect of a putative truncation at these positions would depend on the balance between Ca^{2+} activation at the remaining site and the loss of any gating restrictions.

Assessment of *KCNMA1* HP variants by pathogenicity algorithms

Variant pathogenicity is commonly initially evaluated by tools available in ClinVar, Ensembl, Varsome, and others (Ganakammal & Alexov 2019). The most widely used algorithms are Swift (Ng & Henikoff 2003), Polyphen (Adzhubei et al 2010), CADD/PHRED (Rentzsch et al 2019), MetalLR (Dong et al 2015), M-CAP (Jagadeesh et al 2016), Mutpred2 (Pejaver et al 2017) and REVEL (Ioannidis et al 2016). These genetic algorithms are divided into independent or ensemble predictors (Ganakammal & Alexov 2019). The independent predictors (SIFT, Polyphen, and Mutpred2) analyze the tolerance of

the residue to change by statistical or evolutionary sequence comparison methods (Adzhubei et al 2010, Ng & Henikoff 2003, Pejaver et al 2017). The ensemble predictors-(CADD/PHRED, MetaLR, M-CAP, and REVEL) use combination of independent predictors through machine learning methods (Cameron & Dryer 2000, Dong et al 2015, Ioannidis et al 2016, Jagadeesh et al 2016). While these genetic pathogenicity algorithms appear to perform well for missense variants of less complex structural proteins, these tools may not be adequate to assess mutations in genes encoding ion channels (Holland et al 2017). For example, Polyphen and Mutpred incorporate protein structural information by amino acid residue accessibility or effects over protein structure, respectively. Each uses trained datasets that do not necessarily represent ion channel structural domains such as the voltage sensor, inactivation motifs, ion binding sites, and allosteric pathways. Therefore, existing individual and ensemble tools may be inadequate to assess pathogenicity associated with some genes (Ganakammal & Alexov 2019, Holland et al 2017).

To address this, we evaluated the performance of SIFT, Polyphen, CADD/PHRED, MetaLR, M-CAP, Mutpred and REVEL with 61 nonsynonymous *KCNMA1* variants (frameshift or deletion variants were not included). Four parameters were assessed-specificity, sensitivity, accuracy, and precision using the confirmed pathogenic variants (A172T, A314T, S351Y, G354S, G356S, G375R, C413Y, D434G, H444Q, N449fs, K457E, R458Ter, N536H, G567S, I663V, E736K, P805L, E884K, D984N, N999S, R1083K, R1097H) and benign variants (K518N, E884K, R1128W and N1159S) (Figure 6A). CADD/PHRED, MetaLR, Mutpred and REVEL showed the best predictive capabilities in each parameter, with an average performance metric between the four parameters of 0.78, 0.80, 0.87, and 0.88 respectively (Supplemental Figure 2). Polyphen also showed better

performance than CADD/PHRED and MetaLR (0.81). However, because it is incorporated into the ensemble algorithm REVEL, Polyphen was left out of this analysis.

Surprisingly, evaluation of the pathogenicity score using logistic regression based on confirmed pathogenic and non-pathogenic variants to determine the best cut-off for each of these four algorithms (Figure 6A; see Methods), revealed that that the use of general cut-off is associated with a high false positive rate (Supplemental Figure 2B). This result demonstrates a low discrimination power of the common genetic algorithms between pathogenic and non-pathogenic variants when used with general cut-offs on the known *KCNMA1* dataset.

Development of a structurally-integrated algorithm for *KCNMA1*

To determine if it is possible to increase the performance of the existing algorithms using structural information from this study, we developed a two-step building block strategy that combines pathogenicity algorithms and structural parameters. The first step consists of a weighted summation module (WSM) that incorporates the individual algorithms REVEL (R), Mutpred (MP), MetaLR (MLR), and CADD/PHRED (CP). The WSM value was adjusted by the capability of each algorithm to detect true positive and negative variants. Each individual score was multiplied by the fraction of true positives (pathogenic variants) and divided by the fraction of false positive (false pathogenic variants) that was able to detect and incorporated in the model according to equation 5 (Supplemental Table 1):

5. $A^{WSM} = \sum_{J=1}^{n} w_J \, x_{IJ} = \frac{R*0.7}{0.25} + \frac{MP*1}{0.75} + \frac{MLR*0.4}{0.25} + \frac{CP*0.3}{0.25}$

The second step incorporates the clustering structural information from the BK channel cryo-EM structures in absence and presence of Ca^{2+} (Figure 2 and 3; PDB:6V3G and 6V38) (Hite et al 2017b, Tao et al 2017). The parameters, number of interactions (NI), number of residues (NR), and associated energy of interaction (AE) were averaged from both structures to generate a structural component (SC; Supplemental Table 2). The structural component makes the assumptions that functionally important residues would: 1) be located within a cluster, 2) interact with other residues via hydrogen bonding, π-π stacking, π cation, salt bridge, Van Der Waals or disulphide bond 3) have high energetics of interaction. The first was the average number of residues (NR) at a 5 Å distance from the residue of interest that represent cluster and possible interaction. The second was the average number of interactions (NI) that represent structural stability, and the third was the average energetic value of those interactions (AE). These parameters were combined in the structural component (SC; equation 6):

1. $SC = \frac{NI * AE}{NR}$

For the residues not resolved in the structure or with NI values of 0, we used minimal NR and/or NI values of 1 and the average energy of a hydrogen bond interaction of 18 KJ/mol as AE for the ND and 1 for NI values equal 0 (Supplemental Table 2). These minimal values were used to facilitate evaluation of the complete set of *KCNMA1* HP variants, as well to avoid indeterminates created by a zero term.

The KMS formula is:

$$KMS = WSM * SC$$

In Figure 6A, the variant scores determined by the four pathogenicity algorithms are presented. These variants are already categorized as pathogenic or non-pathogenic, thus they were used to weight each algorithm based on the logistic regression curves of Supplemental Figure 2B. In the receiving operating characteristic curve (ROC), the cut-off associated with a higher true positive detection, as well as a decrease in false positives, was obtained with the WSM (Figure 6B).

Next, incorporation of the structural information with the WSM calculates the 'KMS score'. The cut-off of 2.6 showed a similar true positive detection probability with a reduced false positive rate compared to the WSM alone, compared at 0.4 of 1-specificity for both scores (Figure 6C ROC curve inset). This suggests that the weighted summation of preexisting algorithms, together with the incorporation of structural information, results in an algorithm with better performance for *KCNMA1* HP variants compared to the available ClinVar pathogenicity capabilities.

Electrophysiological evaluation of HP variants delineated by KMS score

We tested the performance of KMS on eight functionally unclassified *KCNMA1* HP variants in two steps: 1) comparing KMS to REVEL, the algorithm that showed the best overall individual performance, and 2) functionally validating HP variants with pathogenic KMS scores on BK channel activity using electrophysiology. In total, six HP variants were predicted pathogenic by KMS but not by REVEL (KMS^+; $REVEL^-$), and two variants were predicted pathogenic by REVEL but not KMS (KMS^-; $REVEL^+$; Figure 7B). Of these, four mutations were tested functionally using electrophysiology: M578T, E656A and D965V (KMS^+; $REVEL^-$) and D800Y (KMS^-; $REVEL^+$). Evaluation these four variants was performed in the context of additional variants that have been previously studied under

different conditions (Meredith 2024, Miller et al 2021), collectively, reporting the functional effects for a total of 13 HP variants under equivalent conditions (Figure 8).

D965V and M578T BK currents showed a strong LOF phenotype for both variants (Figure 8A-C). This LOF effect was large when compared to other LOF variants reported in the literature, such as H444Q (Liang et al 2019, Park et al 2022). Neither D965V nor M578T variants are located within a cluster in the structure; however, these residues were chosen for functional analysis because both are near, or part of, the calcium activation structures. M578T (M513 in the cryoEM structure) is part of the Ca^{2+} binding site in RCK1 (formed by D362 and D367; Figure 7A). M578 was previously mutated to isoleucine in another study, showing a disruption in the Ca^{2+} activation and a LOF phenotype (Bao et al 2004, Bao et al 2002). M578T produces a similar LOF phenotype as M578I with a shift of +34 mV (Figure 8A). The D965 residue is near to the calcium bowl in the RCK2 (DDDDDPD) (Yusifov et al 2008). Previously, the D965A mutation showed no difference from WT between 0 and 100μM Ca^{2+} (Bao et al 2004, Bao et al 2002). However, in this study the HP variant D965V showed a LOF phenotype with a +40 mV shift in the $V_{1/2}$ (Figure 8A). Under these conditions, D965V produces a stronger LOF phenotype than M578T.

The D800Y variant, predicted pathogenic by REVEL but not KMS (Figure 7B), did not show any difference in BK current properties compared to WT (Figure 8). This finding also indicates accordance with KMS over REVEL. However, D800Y is one of the HP variants that cannot be localized in the structure because it lies within the unresolved regions. In this situation, KMS will perform at the detection limit using an arbitrary value for the structural component.

The E656A variant was predicted pathogenic by KMS but not by REVEL (Figure 7B). The residue E656A is in the region between S8 and S9, pointed to the gating ring (Figure 7A). E656A was previously tested, showing no differences compared to WT BK currents in the absence or presence of the accessory subunit β4 (Li et al 2018a), and BK current recordings in this study corroborate the prior findings (Figure 8). Under these testing conditions, the lack of change in BK currents matched the REVEL prediction, yielding a potentially inaccurate categorization by KMS. However, as with all putative benign residues, the effects on expression, protein-protein interactions, and other conditions, remain to be tested.

One other variant (K457E) also predicted non-pathogenic by KMS, but pathogenic by REVEL, was not tested in this study. K457 is in the αB helix of RCK1 (Figure 7A) and interacts with Phosphatidylinositol 4,5-bisphosphate (PIP2) to promote BK channel activation. In a previous study, neutralization of the K457 positive charge (K392N) decreased PIP2 sensitivity and shifted the $V_{1/2}$ to more depolarized potentials (Tang et al 2014). K457 is also implicated in interactions with β subunits, and K457E (K392E, in tandem with an additional mutation R393D) decreased activation of the α-subunit and the β subunit-mediated increase in Ca^{2+} sensitivity (Hou et al 2013, Liu et al 2014). These combined results suggest that K457E is pathogenic and a LOF variant (Buckley et al 2020), and potentially incorrectly categorized as non-pathogenic by the KMS score.

Three additional HP variants L226F, A314T, and I512V were categorized as pathogenic by KMS score, but not REVEL (Figure 7B). The effects of these mutations on BK currents also were not tested in this study. In total, functional electrophysiological testing showed that KMS improved predictions for three residues tested (M578T, D965V, and

D800Y), but did not assess E656A and K457E in accordance with the available functional data.

Discussion

In this work, we mapped *KCNMA1* HP variants with respect to BK channel functional domains, the sites of BK channel modulation, and the open and closed BK channel cryo-EM structures (Hite et al 2017a, Tao et al 2017, Tao & MacKinnon 2019a, Tao & MacKinnon 2019b). The resulting annotated sequence and structures were used to detect commonalities among the locations of HP variants and further develop an ensemble KMS algorithm to augment standard Clinvar pathogenicity assessment. The structural mapping and KMS analyses create a broader basis for understanding GOF and LOF mechanisms and genotype-channel phenotype correlations associated with *KCNMA1*-linked disease than what is currently available.

The combined picture that emerges from the structural variant mapping does not yet predict any variant-specific pharmacology, but new directions for further investigation became apparent. We found that despite producing the strongest genotype-phenotype correlation (Miller et al 2021), there was no clustering, structural, or functional similarities between the 3 variants currently definitively identified as GOF. This suggests that approaches geared toward identifying functional similarities between these variants, both at the BK channel and at the neuronal levels, will be needed to understand the epilepsy and PNKD that are correlated with these variants. It has already been shown that two of these variants (N999S and D434G) can recapitulate seizure and PNKD susceptibility and are associated with increased neuronal activity in mouse models (Dong et al 2022, Park et al 2022). Furthermore, patients harboring the GOF variants N536H and N999S both respond to

stimulant therapy for PNKD (Keros et al 2022, Zhang et al 2020). Since the amphetamine metabolite does not directly affect BK channel activity in either study, and the variants are located in different BK channel domains, the importance of further evaluating the neuronal-level mechanisms produced by these variants is underscored.

In contrast to the rarity of GOF variants and lack of structural themes at the channel level, most LOF variants (80%) localize within 5 to 22 Angstroms of each other. Predictably, most are found within the pore region, which is essential for K^+ selectivity and permeation and largely devoid of non-conservative SNPs. The variants mapping to pore residues overlap with a major region of pharmacological inhibition in the BK channel. Other LOF variants cluster within the AC domain of RCK1, a second domain emerging as an identifiable hotspot of functionally consequential residues. This region also lacks non-conservative SNPs. Interestingly, modulatory sites (H^+, CO and EtOH) in the AC region or RCK1 are close to pathogenic HP variants. However, the effects of the variants over these modulations, or vice versa, have not yet been evaluated. Interestingly, individuals harboring D434G variants have been reported to experience alcohol-induced PNKD (Du et al 2005). Thus, pooling the analysis of GOF and LOF variants with common mechanistic channel properties, located within specific domains, or according to distinguishing symptoms in the individuals harboring these variants could advance genotype-phenotype correlations.

Despite the low number of HP variants that have been functionally confirmed by electrophysiology in the literature, the KMS algorithm showed some initial potential to improve the genetic-based algorithms beyond their individual performances. Incorporation of structural features (residue clustering, interactions, and state-dependence) using KMS resulted in a re-consideration of two REVEL-predicted non-pathogenic VUS residues as pathogenic (M578T and D965V), and one REVEL-predicted pathogenic residue (D800Y) as

non-pathogenic. KMS performed well with residues that are close to regulatory sites such as the calcium bowl (M578T and D965V). KMS also delineated an HP variant in a region not resolved by the cryoEM structure (D800Y). However, this observation lacks structural information and the WSM score also predicts such residues as non-pathogenic. Similarly, VUS G20D (located in the N-terminus, but not resolved in the cryoEM) is predicted nonpathogenic. Consistent with this, our electrophysiology recordings also showed no difference compared to WT (Figure 8). However, more functional testing is necessary to improve the KMS algorithm for additional HP variants located in unresolved regions. The modularity of KMS was designed to evolve with improved genetic analysis and structural resolution, which only involves replacing terms in the equation with new modules as the component algorithms are improved.

Pathogenicity analysis in other ion channelopathies has required similar approaches (Cinier et al 2020, Holland et al 2017, Tang et al 2020), but despite the evolution, there are global and gene-specific limitations. Those limitations for KMS are mainly related with the structural information and how the component factors are incorporated. Despite the assumption of a minimal interaction taken as the lowest NI (number of interactions), NR (number of residues) and AE (average energy) values, this is only true if these regions are disorganized with one interaction and no possibilities or others. In the case of interactions or proximity with other residues, the prediction could change for KMS, but not for WMS, since it is the only component in the score that accounts for it. Also, in the case of the structural components, functionally important pair interactions will be underemphasized in the NR term. This could be partially solved with a term that accounts for the folding impact of a given mutation, helping to discard neighbor interactions. Additionally, residues within binding sites such as N237K (part of the Mg^{2+} binding site) (Yang et al 2007, Yang et al

2013) and K457E (PIP2 binding site) are difficult to incorporate into the equation in its present form without affecting the data dichotomization and cut-off determination. In the same line, the limited training data set, composed of 15 pathogenic and 4 non-pathogenic residues, could underestimate the performance of some scores, penalizing them in the WSM and affecting the logistic regression dichotomization. Other limitations relevant to BK channel pathogenicity prediction are not restricted to KMS (ie they are also present in CADD/PHRED, MetaLR, Mutpred and REVEL), such as the inability to predict transcript abundance or channel expression defects. However, KMS could potentially incorporate an expression-based module in future iterations, derived from in silico sequence prediction or from direct functional expression studies.

Another consideration is the relevance to in vivo pathogenicity. Most *KCNMA1* HP variants are heterozygous alleles (97%). This scenario could create heterotetramerization between WT and mutant subunits (Geng et al 2021), potentially decreasing or altering the pathogenic phenotype, depending on the pathological mechanism and its degree of dominance. This was observed for BK^{R207Q} GOF channels co-expressed with BK^{WT} (Montgomery & Meredith 2011) as well as in the A172T, A314T, G375R, N536H and N999S (Liang et al 2022). Interestingly, G375R showed a 40% reduction in the unitary conductance as homotetramer (LOF), but co-expression with WT produced a massive 130 mV negative shift in the $V_{1/2}$ (in 0 Ca^{2+}), denoting a GOF alteration (Geng et al 2023).

Lastly, KMS calculations, as well as the other algorithms, are binary. The score magnitude is not associated with the degree of pathogenicity and will not predict results in the context of heterozygous alleles in vivo. In this way, the ideal full computational pathogenicity assessment would incorporate genetic, structural, functional, and neuronal evidence into an ensemble predictor tool. This type of ensemble analysis is increasingly being

developed in a gene- and disease-specific context (Borges et al 2021, Crockett et al 2012, Ellard et al 2020, Evans et al 2019, Holland et al 2017, Zhang et al 2021). Most ion channelopathies face similar challenges in their classification as rare diseases as those faced in *KCNMA1* channelopathy (Kim, 2014). Several studies affirm that these aforementioned tools fail to accurately assess pathogenicity for certain classes of proteins, including some ion channels (Borges et al 2021, Crockett et al 2012, Ellard et al 2020, Evans et al 2019, Zhang et al 2021). The detection pitfalls mainly result from the use of a specific threshold generated from true positive (sensitivity) versus false positive (1-specificity) receiver operating characteristic (ROC) curves, using non-optimal datasets to generate binary classifications of pathogenic (1) and non-pathogenic (0) (Ellard et al 2020, Ganakammal & Alexov 2019). Individual algorithms that use genetic or amino acid sequence datasets miss unique motifs in ion channels like regulatory elements, 'non-shaker' voltage sensing domains and other gating elements (Carrasquel-Ursulaez et al 2022), regulatory binding sites (Zeng et al 2005), and residues relevant for the interface interactions in multimeric complexes (Zheng 2013). This is most relevant for ion channels defined by a single family member or those with low homology regions across genomes. Meanwhile the ensemble algorithms do not include a threshold correction, leading to the loss of control over Type I error (rejection of null when true) and the wrong identification of non-pathogenic variants as pathogenic (Type II error, failure to reject null when false). Together these errors contribute to identifying pathogenic variants as non-pathogenic (Ganakammal & Alexov 2019). More recently, the sodium channel channelopathies (as with other genetic diseases) have addressed these issues recalculating the pathogenicity threshold of different scores using data from *SCN*1A, 2A and 8A-specific patients, improving the disease driven variants (Holland et al 2017). Thus, the development of new algorithms, or improvement of standard ones, has the

potential to push a better predictor performance toward faster genotype-phenotype categorizations.

Acknowledgements: We gratefully acknowledge patients, families, and physicians for their participation in the KCNMA1 Channelopathy International Advocacy Foundation (KCIAF) registry questionnaire or providing direct submission information, and Alyssa Mendel and the Coordination of Rare Diseases at Sanford (CoRDS) program for providing patient registry data collation and access.

Funding: This work was supported by NHLBI R01-HL102758 (A.L.M.), the Training Program in Integrative Membrane Biology NIGMS T32-GM008181 (A.L.M.), and the 2021 Biophysics of Health and Disease Award from the Biophysical Society (A.L.M.).

Author contribution

HJM: research conception and data collection, statistical analysis design and execution, and manuscript writing. KT: research conception, data collection, and manuscript writing. ALM: research conception and data analysis, statistical analysis design, and manuscript writing.

Figure legends

Figure 1. Structural localization of *KCNMA1* HP variants. (A) Fifty-three patient-associated *KCNMA1* variants (black globular residues) are depicted in the calcium-bound human BK channel alpha subunit, with either two (A) or four subunits (B; Cryo-EM PDB ID: 6V38). Voltage sensing domain (VSD; green), pore domain (PD; orange), and gating ring (RCK1: light blue and RCK2: yellow). (C-D) Top (C) and bottom (D) view of the BK channel tetramer. Residues 1-18, 51-93, 614-683, 834-870 and 1057-1111 are not shown due to location in unresolved or deleted segments.

Figure 2. Clustering analysis of LOF and GOF HP variants. (A) Fifteen LOF (blue) and 3 GOF (red) variants mapped on the calcium bound BK channel. (B) Top view of the BK channel tetramer. (C) Magnification view of the gating ring showing the proximity of the GOF variants D434G and N536H to the RCK1 Ca^{2+} binding site. Dashed line measures distance in Å. (D) Magnification of the gating ring showing the proximity of the LOF variants D965V and D984N to the RCK2 Ca^{2+} bowl.

Figure 3. Distribution of non-synonymous SNPs by domain. (A) Localization of 60 SNPs (ice blue) alongside the GOF (red) and LOF (blue) HP variants in a two subunit-view configuration. (B) Side view tetramer representation. (C-D) Top and bottom (D) views. The Ca^{2+} binding sites at RCK1 and RCK2 (magenta circles) are located behind the area where SNPs R341, V370 and D371 (RCK1) and L447 and P451 (RCK2) are located.

Figure 4. Sites of BK channel modulation and HP variants. (A) Charybdotoxin (ChTX), iberiotoxin (IbTX), loperamide (LOP), and paxilline (PAX) antagonist modulation sites are depicted in cyan. BC5, Cym04, NS1619, and NS11201 agonist modulation sites are shown

in purple. Endogenous modulator sites (Heme, protons (H^+), lipids, carbon monoxide (CO) and ethanol (EtOH)) are depicted in orange. 17 LOF (blue) and 3 GOF (red) HP variants are represented as globular residues. (B) Lateral two-subunit side view with domain representation: PD (orange), VSD (green), RCK1 (light blue) and RCK2 (yellow). (C-E) Four-fold symmetry representations from the side (C), bottom (D), and top (E).

Figure 5. HP patient variants creating premature stop codons. (A) R458Ter translation terminates at the end of the AC domain. (B) R640Ter terminates in RCK1 before the alternative splice site 1. (C) The R830Ter and (D) R880Ter terminations occur before and after S9, respectively, prior to the calcium bowl located in the RCK2. (E) Slo1C truncated BK channel. Slo1C also includes a Kv1.4 tail of either 74 or 11 amino acid residues (Budelli et al 2013), which is not shown in the structural representation. (D) SloΔRCK2 is an in silico truncated BK channel for reference, showing the boundaries of RCK1 and RCK2.

Figure 6. *KCNMA1* Meta Score (KMS). (A) Individual and ensemble scores for pathogenic HP variants: LOF (blue), GOF (red), and benign (green). Standard cut-offs for each algorithm were: CADD/Phred, 20; MetaLR, 0.5; Mutpred, 0.25; REVEL, 0.5; Weighted Summation Model (WSM), 2.4; and KCNMA1 Meta Score (KMS), 2.6. (B) Logistical regression and ROC for the weighted summation model (WSM) based on specificity and precision. (C) Logistical regression for KMS that consists of WSM multiplied by the structural component (SC). Dotted lines depicted in each plot are the cut-off selected from the ROC curve corresponding to a true positive of 88% (sensitivity) and 45% false positive rate (1-specificity).

Figure 7. VUS residues with conflicting KMS and REVEL categorizations. (A) Pathogenic (red) and non-pathogenic (black) variants according to KMS (left panel) versus REVEL (right). Ca^{2+}-bound human BK channel cryo-EM. K^+, green; Ca^{2+}, orange; and Mg^{2+}, blue. D800Y is not depicted because it is located in an unresolved structural region. (B) KMS and REVEL algorithm scores. The KMS cut-off was 2.6 and REVEL 0.5.

Figure 8. Electrophysiological characterization of *KCNMA1* HP variants. (A) Conductance versus voltage relationship curves of the WT and 13 patient variants in the human BK channel. Inside-out patch-clamp recordings were conducted in a physiological K^+ gradient and 10 μM intracellular Ca^{2+} conditions. Data average ± SEM are plotted with Boltzmann fits. WT (black): 29±3 (N=27). GOF (red): D434G 8 ±3 (N=12, P<0.0001), N999S -15±2 (N=14, P<0.0001), and N999S/R1128W -8±7 (N=7, P<0.0001). LOF: H444Q 52 ±3 (N=13, P<0.01), M578T 65±3 (N=19, P<0.0001), and D965V 69±5 (N=10, P<0.0001). VUS/no effect (gray): G20D 20±4 (N=9, P=0.769), E656A 12±2 (N=13, P=0.017), I663V 15±6 (N=11, P=0.131), D800Y 21±5 (N=10, P=0.198), E884K 39±2 (N=6, P+0.100), R1097H 21±5 (N=14, P<0.0001), and R1128W 51±8 (N=5, P=0.068). (B) Activation kinetics at +30mV, a voltage relevant during neuronal activity. (C) Deactivation kinetics at -70mV, approximating an average neuronal resting membrane potential. For B-C, individual data points ± SEM are plotted.

References

Adzhubei IA, Schmidt S, Peshkin L, Ramensky VE, Gerasimova A, et al. 2010. A method and server for predicting damaging missense mutations. *Nat Methods* 7: 248-9

Bailey CS, Moldenhauer HJ, Park SM, Keros S, Meredith AL. 2019. *KCNMA1*-linked channelopathy. *J Gen Physiol* 151: 1173-89

Bao L, Kaldany C, Holmstrand EC, Cox DH. 2004. Mapping the BK_{Ca} channel's 'Ca^{2+} bowl': side-chains essential for Ca^{2+} sensing. *J Gen Physiol* 123: 475-89

Bao L, Rapin AM, Holmstrand EC, Cox DH. 2002. Elimination of the BK_{Ca} channel's high-affinity Ca^{2+} sensitivity. *J Gen Physiol* 120: 173-89

Borges P, Pasqualim G, Matte U. 2021. Which Is the Best In Silico Program for the Missense Variations in IDUA Gene? A Comparison of 33 Programs Plus a Conservation Score and Evaluation of 586 Missense Variants. *Front Mol Biosci* 8: 752797

Brenner R, Jegla TJ, Wickenden A, Liu Y, Aldrich RW. 2000. Cloning and functional characterization of novel large conductance calcium-activated potassium channel beta subunits, hKCNMB3 and hKCNMB4. *Journal Biological Chemistry* 275: 6453-61

Buckley C, Williams J, Munteanu T, King M, Park SM, Meredith AL, Lynch T. 2020. Status Dystonicus, Oculogyric Crisis and Paroxysmal Dyskinesia in a 25 Year-Old Woman with a Novel *KCNMA1* Variant, K457E. *Tremor Other Hyperkinet Mov* 10: 49

Budelli G, Geng Y, Butler A, Magleby KL, Salkoff L. 2013. Properties of *Slo1* K^+ channels with and without the gating ring. *Proc Natl Acad Sci* 110: 16657-62

Bukiya AN, Kuntamallappanavar G, Edwards J, Singh AK, Shivakumar B, Dopico AM. 2014. An alcohol-sensing site in the calcium- and voltage-gated, large conductance potassium (BK) channel. *Proc Natl Acad Sci* 111: 9313-8

Cameron JS, Dryer SE. 2000. BK-Type K(Ca) channels in two parasympathetic cell types: differences in kinetic properties and developmental expression. *J Neurophysiol* 84: 2767-76

Carrasquel-Ursulaez W, Segura I, Diaz-Franulic I, Echeverria F, Lorenzo-Ceballos Y, et al. 2022. Mechanism of voltage sensing in Ca^{2+}- and voltage-activated K^+ (BK) channels. *Proc Natl Acad Sci* 119: e2204620119

Cinier G, Tse G, Baranchuk A. 2020. Brugada phenocopies: Current evidence, diagnostic algorithms and a perspective for the future. *Turk Kardiyol Dern Ars* 48: 158-66

Clementel D, Del Conte A, Monzon AM, Camagni GF, Minervini G, et al. 2022. RING 3.0: fast generation of probabilistic residue interaction networks from structural ensembles. *Nucleic acids research* 50: W651-6

Crockett DK, Lyon E, Williams MS, Narus SP, Facelli JC, Mitchell JA. 2012. Utility of gene-specific algorithms for predicting pathogenicity of uncertain gene variants. *J Am Med Inform Assoc* 19: 207-11

Crouzy S, Berneche S, Roux B. 2001. Extracellular blockade of K^+ channels by TEA: results from molecular dynamics simulations of the KcsA channel. *J Gen Physiol* 118: 207-18.

Dong C, Wei P, Jian X, Gibbs R, Boerwinkle E, et al. 2015. Comparison and integration of deleteriousness prediction methods for nonsynonymous SNVs in whole exome sequencing studies. *Human molecular genetics* 24: 2125-37

Dong P, Zhang Y, Hunanyan AS, Mikati MA, Cui J, Yang H. 2022. Neuronal mechanism of a BK channelopathy in absence epilepsy and dyskinesia. *Proc Natl Acad Sci* 119: e2200140119

Doyle DA, Morais Cabral J, Pfuetzner RA, Kuo A, Gulbis JM, et al. 1998. The structure of the potassium channel: molecular basis of K+ conduction and selectivity. *Science* 280: 69-77

Du W, Bautista JF, Yang H, Diez-Sampedro A, You SA, et al. 2005. Calcium-sensitive potassium channelopathy in human epilepsy and paroxysmal movement disorder. *Nat Genet* 37: 733-8

Du X, Carvalho-de-Souza JL, Wei C, Carrasquel-Ursulaez W, Lorenzo Y, et al. 2020. Loss-of-function BK channel mutation causes impaired mitochondria and progressive cerebellar ataxia. *Proc Natl Acad Sci* 117: 6023-34

Dworetzky SI, Trojnacki JT, Gribkoff VK. 1994. Cloning and expression of a human large-conductance calcium-activated potassium channel. *Brain Res Mol Brain Res* 27: 189-93

Ellard S, Colclough K, Patel KA, Hattersley AT. 2020. Prediction algorithms: pitfalls in interpreting genetic variants of autosomal dominant monogenic diabetes. *The Journal of clinical investigation* 130: 14-16

Evans P, Wu C, Lindy A, McKnight DA, Lebo M, et al. 2019. Genetic variant pathogenicity prediction trained using disease-specific clinical sequencing data sets. *Genome research* 29: 1144-51

Ferruz N, Schmidt S, Hocker B. 2021. ProteinTools: a toolkit to analyze protein structures. *Nucleic acids research* 49: W559-W66

Ganakammal SR, Alexov E. 2019. Evaluation of performance of leading algorithms for variant pathogenicity predictions and designing a combinatory predictor method: application to Rett syndrome variants. *PeerJ* 7: e8106

Geng Y, Deng Z, Zhang G, Budelli G, Butler A, et al. 2020. Coupling of Ca^{2+} and voltage activation in BK channels through the alphaB helix/voltage sensor interface. *Proc Natl Acad Sci U S A* 117: 14512-21

Geng Y, Li P, Butler A, Wang B, Salkoff L, Magleby KL. 2023. BK channels of five different subunit combinations underlie the de novo KCNMA1 G375R channelopathy. *J Gen Physiol* 155

Gessner G, Cui YM, Otani Y, Ohwada T, Soom M, et al. 2012. Molecular mechanism of pharmacological activation of BK channels. *Proc Natl Acad Sci* 109: 3552-7

Giraldez T, Hughes TE, Sigworth FJ. 2005. Generation of functional fluorescent BK channels by random insertion of GFP variants. *J Gen Physiol* 126: 429-38

GuohuiZhang, Xianjin Xu, Zhiguang Jia, Yanyan Geng, HL, JS, MM, CA, et al. 2022. An allosteric agonist activates BK channels by perturbing coupling between Ca^{2+} binding and pore opening. Nat Comm 13(1):6784

Hite RK, Tao X, MacKinnon R. 2017a. Structural basis for gating the high-conductance Ca^{2+}-activated K^{+} channel. *Nature* 541: 52-57

Hite RK, Tao X, MacKinnon R. 2017b. Structural basis for gating the high-conductance Ca^{2+}-activated K^+ channel. *Nature* 541: 52-57

Holland KD, Bouley TM, Horn PS. 2017. Comparison and optimization of in silico algorithms for predicting the pathogenicity of sodium channel variants in epilepsy. *Epilepsia* 58: 1190-98

Hou P, Zeng W, Gan G, Lv C, Guo X, et al. 2013. Inter-alpha/beta subunits coupling mediating pre-inactivation and augmented activation of BKCa(beta2). *Scientific reports* 3: 1666

Hou S, Heinemann SH, Hoshi T. 2009. Modulation of BKCa channel gating by endogenous signaling molecules. *Physiology* 24: 26-35

Hou S, Xu R, Heinemann SH, Hoshi T. 2008. The RCK1 high-affinity Ca^{2+} sensor confers carbon monoxide sensitivity to Slo1 BK channels. *Proc Natl Acad Sci* 105: 4039-43

Ioannidis NM, Rothstein JH, Pejaver V, Middha S, McDonnell SK, et al. 2016. REVEL: An Ensemble Method for Predicting the Pathogenicity of Rare Missense Variants. *American journal of human genetics* 99: 877-85

Jagadeesh KA, Wenger AM, Berger MJ, Guturu H, Stenson PD, et al. 2016. M-CAP eliminates a majority of variants of uncertain significance in clinical exomes at high sensitivity. *Nat Genet* 48: 1581-86

Keros S, Heim J, Hakami W, Zohar-Dayan E, Ben-Zeev B, Grinspan Z, Kruer MC, Meredith AL. 2022. Lisdexamfetamine therapy in paroxysmal non-kinesigenic dyskinesia associated with the *KCNMA1*-N999S variant. *Movement Disorders Clinical Practice* 9: 229–35

Kratschmer P, Lowe SA, Buhl E, Chen KF, Kullmann DM, et al. 2021. Impaired Pre-Motor Circuit Activity and Movement in a Drosophila Model of *KCNMA1*-Linked Dyskinesia. *Mov Disord* 36: 1158-69

Krishnamoorthy G, Shi J, Sept D, Cui J. 2005. The NH2 terminus of RCK1 domain regulates Ca^{2+}-dependent BK_{Ca} channel gating. *J Gen Physiol* 126: 227-41

Lenaeus MJ, Vamvouka M, Focia PJ, Gross A. 2005. Structural basis of TEA blockade in a model potassium channel. *Nat Struct Mol Biol* 12: 454-9

Li X, Poschmann S, Chen Q, Fazeli W, Oundjian NJ, et al. 2018a. De novo BK channel variant causes epilepsy by affecting voltage gating but not Ca^{2+} sensitivity. *European journal of human genetics : EJHG* 26: 220-29

Li X, Poschmann S, Chen Q, Fazeli W, Oundjian NJ, et al. 2018b. De novo BK channel variant causes epilepsy by affecting voltage gating but not Ca^{2+} sensitivity. *European journal of human genetics* 26: 220-29

Liang L, Li X, Moutton S, Schrier Vergano SA, Cogne B, et al. 2019. *De novo* loss-of-function *KCNMA1* variants are associated with a new multiple malformation syndrome and a broad spectrum of developmental and neurological phenotypes. *Human molecular genetics*

Liang L, Liu H, Bartholdi D, van Haeringen A, Fernandez-Jaen A, et al. 2022. Identification and functional analysis of two new de novo *KCNMA1* variants associated with Liang-Wang syndrome. *Acta Physiol* e13800

Liu HW, Hou PP, Guo XY, Zhao ZW, Hu B, et al. 2014. Structural basis for calcium and magnesium regulation of a large conductance calcium-activated potassium channel with beta1 subunits. *J Biol Chem* 289: 16914-23

Maljkovic MM. 2019. DistAA: Database of amino acid distances in proteins and web application for statistical review of distances. *Comput Biol Chem* 83: 107130

McCobb DP, Fowler NL, Featherstone T, Lingle CJ, Saito M, et al. 1995. A human calcium-activated potassium channel gene expressed in vascular smooth muscle. *Am J Physiol* 269: H767-77

McKay MC, Dworetzky SI, Meanwell NA, Olesen SP, Reinhart PH, et al. 1994. Opening of large-conductance calcium-activated potassium channels by the substituted benzimidazolone NS004. *J Neurophysiol* 71: 1873-82

Meredith AL. 2024. BK Channelopathies and *KCNMA1*-Linked Disease Models. *Annu Rev Physiol* 86 (in press).

Miller JP, Moldenhauer HJ, Keros S, Meredith AL. 2021. An emerging spectrum of variants and clinical features in *KCNMA1*-linked channelopathy. *Channels* 15: 447-64

Moldenhauer HJ, Matychak KK, Meredith AL. 2020. Comparative gain-of-function effects of the *KCNMA1*-N999S mutation on human BK channel properties. *J Neurophysiol* 123: 560-70

Montgomery JR, Meredith AL. 2012. Genetic activation of BK currents in vivo generates bidirectional effects on neuronal excitability. Proc Natl Acad Sci 109(46):18997-9002

Ng PC, Henikoff S. 2003. SIFT: Predicting amino acid changes that affect protein function. *Nucleic acids research* 31: 3812-4

Niu X, Qian X, Magleby KL. 2004. Linker-gating ring complex as passive spring and Ca^{2+}-dependent machine for a voltage- and Ca^{2+}-activated potassium channel. *Neuron* 42: 745-56

Pallanck L, Ganetzky B. 1994. Cloning and characterization of human and mouse homologs of the Drosophila calcium-activated potassium channel gene, slowpoke. *Human molecular genetics* 3: 1239-43

Pape S, Hoffgaard F, Hamacher K. 2010. Distance-dependent classification of amino acids by information theory. *Proteins* 78: 2322-8

Park SM, Roache CE, Iffland PH, Moldenhauer HJ, Matychak KK, Crino PB, Meredith AL. 2022. BK channel properties correlate with neurobehavioral severity in three *KCNMA1*-linked channelopathy mouse models. *eLife* 11: e77953

Pejaver V, Urresti J, Lugo-Martinez J, Pagel KA, Lin GN, et al. 2017. MutPred2: inferring the molecular and phenotypic impact of amino acid variants. *BioRxiv*: 134981

Plante AE, Lai MH, Lu J, Meredith AL. 2019. Effects of Single Nucleotide Polymorphisms in Human *KCNMA1* on BK Current Properties. *Frontiers in molecular neuroscience* 12: 285

Qiu S, Yi H, Liu H, Cao Z, Wu Y, Li W. 2009. Molecular Information of charybdotoxin blockade in the large conductance calcium-activated potassium channel. *J Chem Inf Model* 49: 1831-8

Rentzsch P, Witten D, Cooper GM, Shendure J, Kircher M. 2019. CADD: predicting the deleteriousness of variants throughout the human genome. *Nucleic acids research* 47: D886-D94

Rockman ME, Vouga AG, Rothberg BS. 2020. Molecular mechanism of BK channel activation by the smooth muscle relaxant NS11021. *J Gen Physiol* 152

Samudrala R, Moult J. 1998. Determinants of side chain conformational preferences in protein structures. *Protein Eng* 11: 991-7

Schreiber M, Salkoff L. 1997. A novel calcium-sensing domain in the BK channel. *Biophys J* 73: 1355-63

Tabarki B, AlMajhad N, AlHashem A, Shaheen R, Alkuraya FS. 2016. Homozygous *KCNMA1* mutation as a cause of cerebellar atrophy, developmental delay and seizures. *Hum Genet* 135: 1295-98

Tang B, Li B, Gao LD, He N, Liu XR, et al. 2020. Optimization of in silico tools for predicting genetic variants: individualizing for genes with molecular sub-regional stratification. *Brief Bioinform* 21: 1776-86

Tang QY, Zhang Z, Meng XY, Cui M, Logothetis DE. 2014. Structural determinants of phosphatidylinositol 4,5-bisphosphate (PIP2) regulation of BK channel activity through the RCK1 Ca^{2+} coordination site. *J Biol Chem* 289: 18860-72

Tang XD, Xu R, Reynolds MF, Garcia ML, Heinemann SH, Hoshi T. 2003. Haem can bind to and inhibit mammalian calcium-dependent Slo1 BK channels. *Nature* 425: 531-5

Tao X, Hite RK, MacKinnon R. 2017. Cryo-EM structure of the open high-conductance Ca^{2+}-activated K^+ channel. *Nature* 541: 46-51

Tao X, MacKinnon R. 2019a. Molecular structures of the human Slo1 K^+ channel in complex with beta4. *eLife* 8

Tao X, MacKinnon R. 2019b. Molecular structures of the human Slo1 K^+ channel in complex with beta4. *eLife* 8

Uhlen M, Fagerberg L, Hallstrom BM, Lindskog C, Oksvold P, et al. 2015. Proteomics. Tissue-based map of the human proteome. *Science* 347: 1260419

Vouga AG, Rockman ME, Jacobson MA, Rothberg BS. 2019. Mechanism of BK Channel Inhibition by the Opioid Agonist Loperamide. *Biophys J* 116: 543a

Wang B, Rothberg BS, Brenner R. 2009a. Mechanism of increased BK channel activation from a channel mutation that causes epilepsy. *J Gen Physiol* 133: 283-94

Wang B, Rothberg BS, Brenner R. 2009b. Mechanism of increased BK channel activation from a channel mutation that causes epilepsy. *J Gen Physiol* 133: 283-94

Xia XM, Zhang X, Lingle CJ. 2004. Ligand-dependent activation of Slo family channels is defined by interchangeable cytosolic domains. *J Neurosci* 24: 5585-91

Yan J, Olsen JV, Park KS, Li W, Bildl W, et al. 2008. Profiling the phospho-status of the BK_{Ca} channel alpha subunit in rat brain reveals unexpected patterns and complexity. *Mol Cell Proteomics* 7: 2188-98

Yang H, Hu L, Shi J, Delaloye K, Horrigan FT, Cui J. 2007. Mg^{2+} mediates interaction between the voltage sensor and cytosolic domain to activate BK channels. *Proceedings of the National Academy of Sciences* 104: 18270-5

Yang J, Krishnamoorthy G, Saxena A, Zhang G, Shi J, et al. 2010. An epilepsy/dyskinesia-associated mutation enhances BK channel activation by potentiating Ca^{2+} sensing. *Neuron* 66: 871-83

Yang J, Yang H, Sun X, Delaloye K, Yang X, et al. 2013. Interaction between residues in the Mg^{2+}-binding site regulates BK channel activation. *J Gen Physiol* 141: 217-28

Yesil G, Aralasmak A, Akyuz E, Icagasioglu D, Uygur Sahin T, Bayram Y. 2018. Expanding the Phenotype of Homozygous *KCNMA1* Mutations; Dyskinesia, Epilepsy, Intellectual Disability, Cerebellar and Corticospinal Tract Atrophy. *Balkan Med J* 35: 336-39

Yu M, Liu SL, Sun PB, Pan H, Tian CL, Zhang LH. 2016. Peptide toxins and small-molecule blockers of BK channels. *Acta pharmacologica Sinica* 37: 56-66

Yusifov T, Savalli N, Gandhi CS, Ottolia M, Olcese R. 2008. The RCK2 domain of the human BKCa channel is a calcium sensor. *Proc Natl Acad Sci* 105: 376-81

Zeng XH, Xia XM, Lingle CJ. 2005. Divalent cation sensitivity of BK channel activation supports the existence of three distinct binding sites. *J Gen Physiol* 125: 273-86

Zhang G, Gibson RA, McDonald M, Liang P, Kang PW, et al. 2020. A Gain-of-Function Mutation in *KCNMA1* Causes Dystonia Spells Controlled With Stimulant Therapy. *Mov Disord* 35: 1868-73

Zhang G, Huang SY, Yang J, Shi J, Yang X, et al. 2010. Ion sensing in the RCK1 domain of BK channels. *Proc Natl Acad Sci U S A* 107: 18700-5

Zhang X, Walsh R, Whiffin N, Buchan R, Midwinter W, et al. 2021. Disease-specific variant pathogenicity prediction significantly improves variant interpretation in inherited cardiac conditions. *Genet Med* 23: 69-79

Zheng J. 2013. Domain-domain interactions in ion channels. *J Gen Physiol* 142: 347-50

Zhou Y, Xia XM, Lingle CJ. 2020. The functionally relevant site for paxilline inhibition of BK channels. *Proc Natl Acad Sci* 117: 1021-26

Figure 1

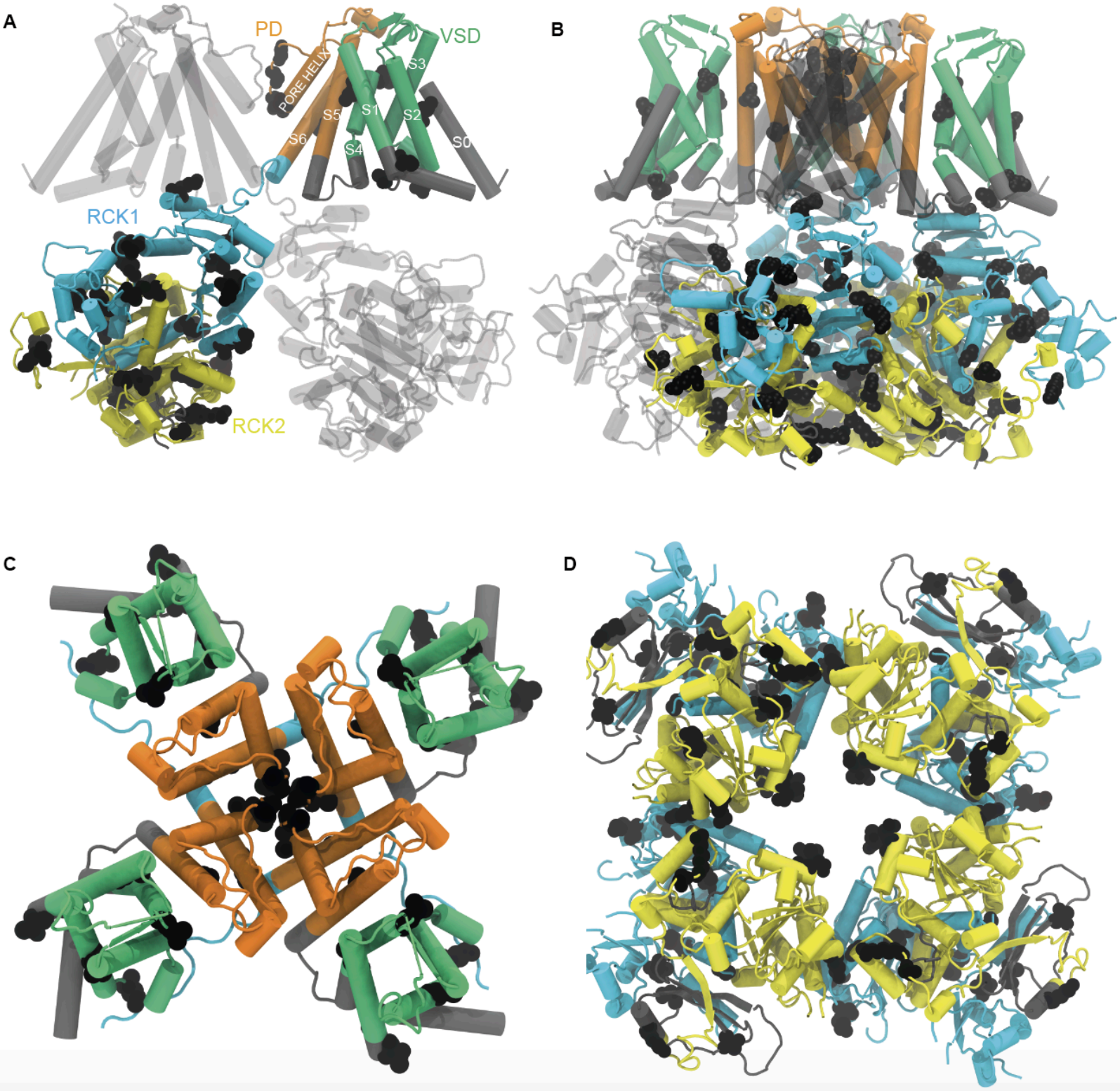

Figure 2

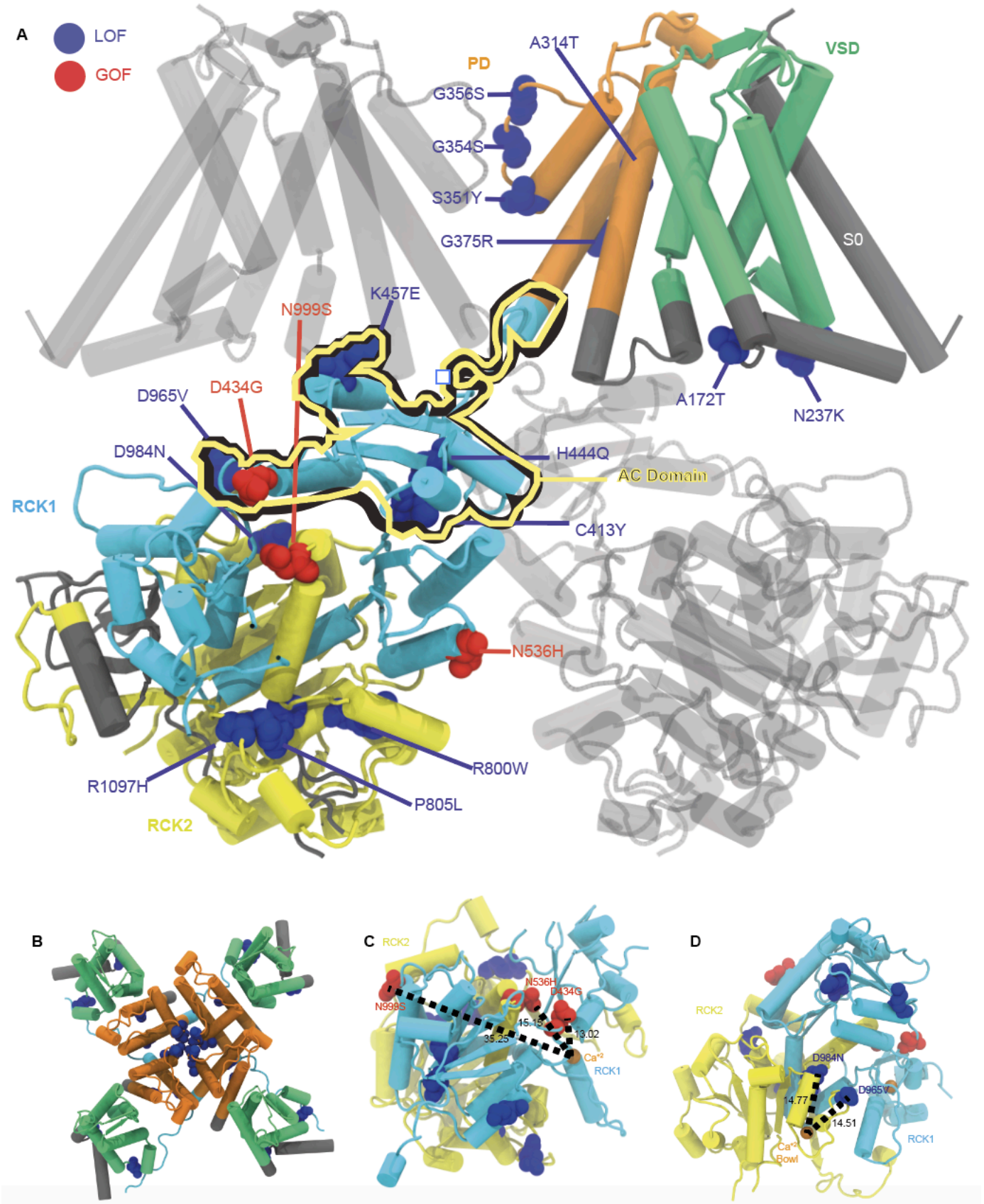
A
LOF
GOF
PD
VSD
A314T
G356S
G354S
S351Y
G375R
S0
K457E
N999S
D965V
D434G
A172T
N237K
D984N
H444Q
AC Domain
RCK1
C413Y
N536H
R800W
R1097H
P805L
RCK2
B
C
RCK2
N536H
D434G
N999S
15.15
13.02
35.25
Ca+2
RCK1
D
RCK2
D984N
D965V
14.77
14.51
Ca+2
Bowl
RCK1

Figure 3

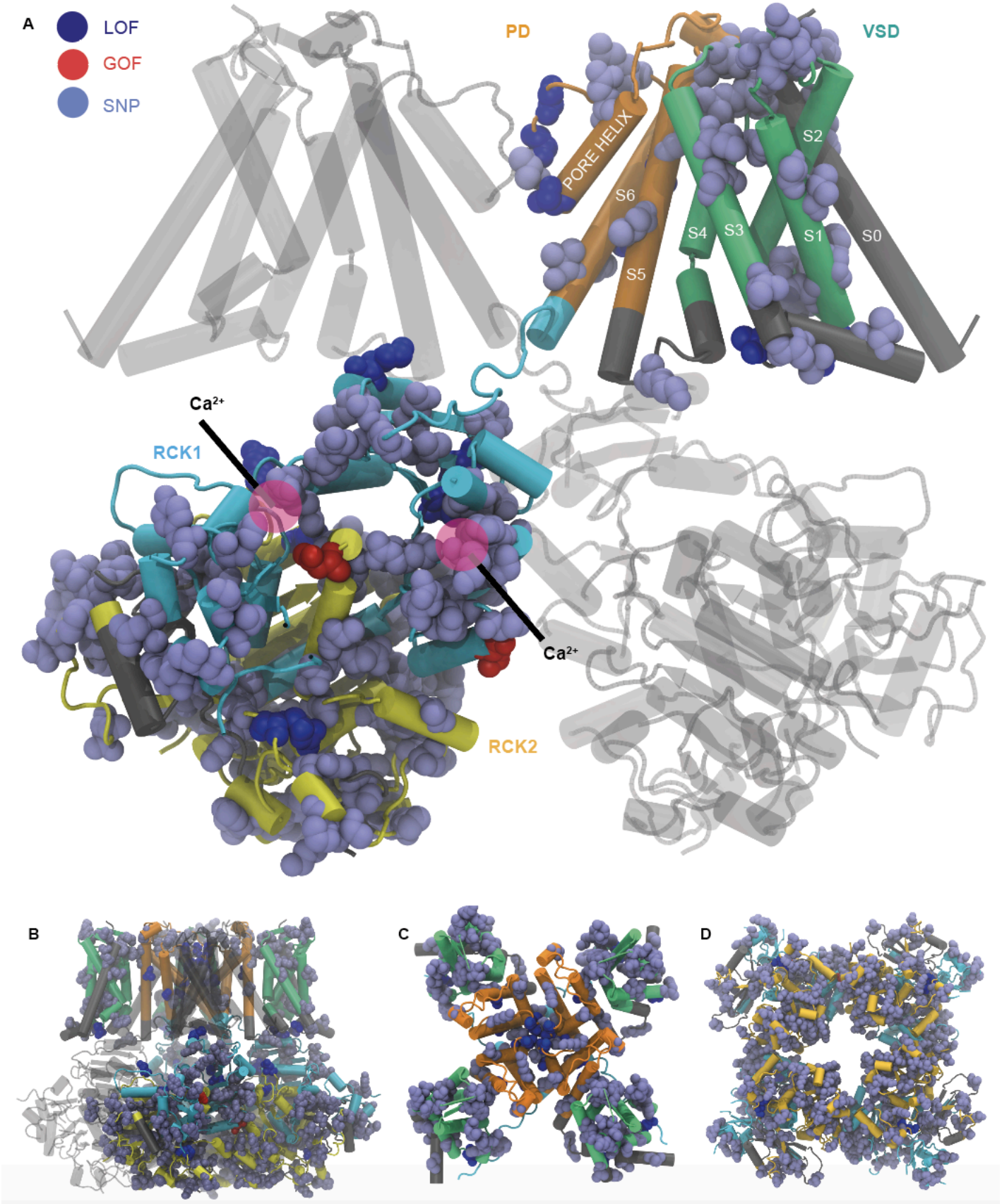
A
LOF
GOF
SNP
PD
VSD
PORE HELIX
S6
S5
S4
S3
S2
S1
S0
Ca2+
RCK1
Ca2+
RCK2
B
C
D

Figure 4

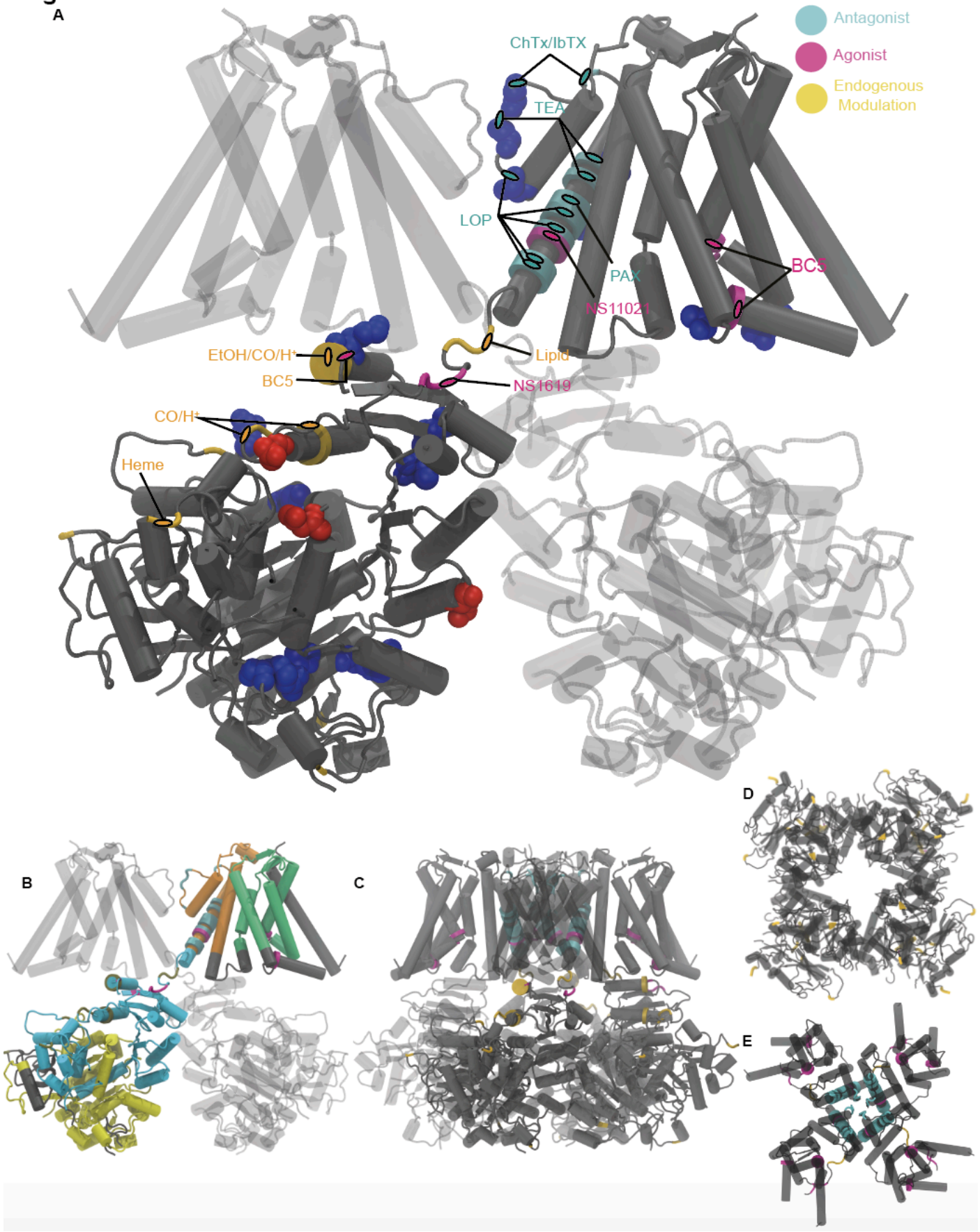
A
Antagonist
Agonist
Endogenous Modulation
ChTx/IbTX
TEA
LOP
PAX
NS11021
BC5
EtOH/CO/H+
BC5
Lipid
NS1619
CO/H+
Heme
B
C
D
E

Figure 5

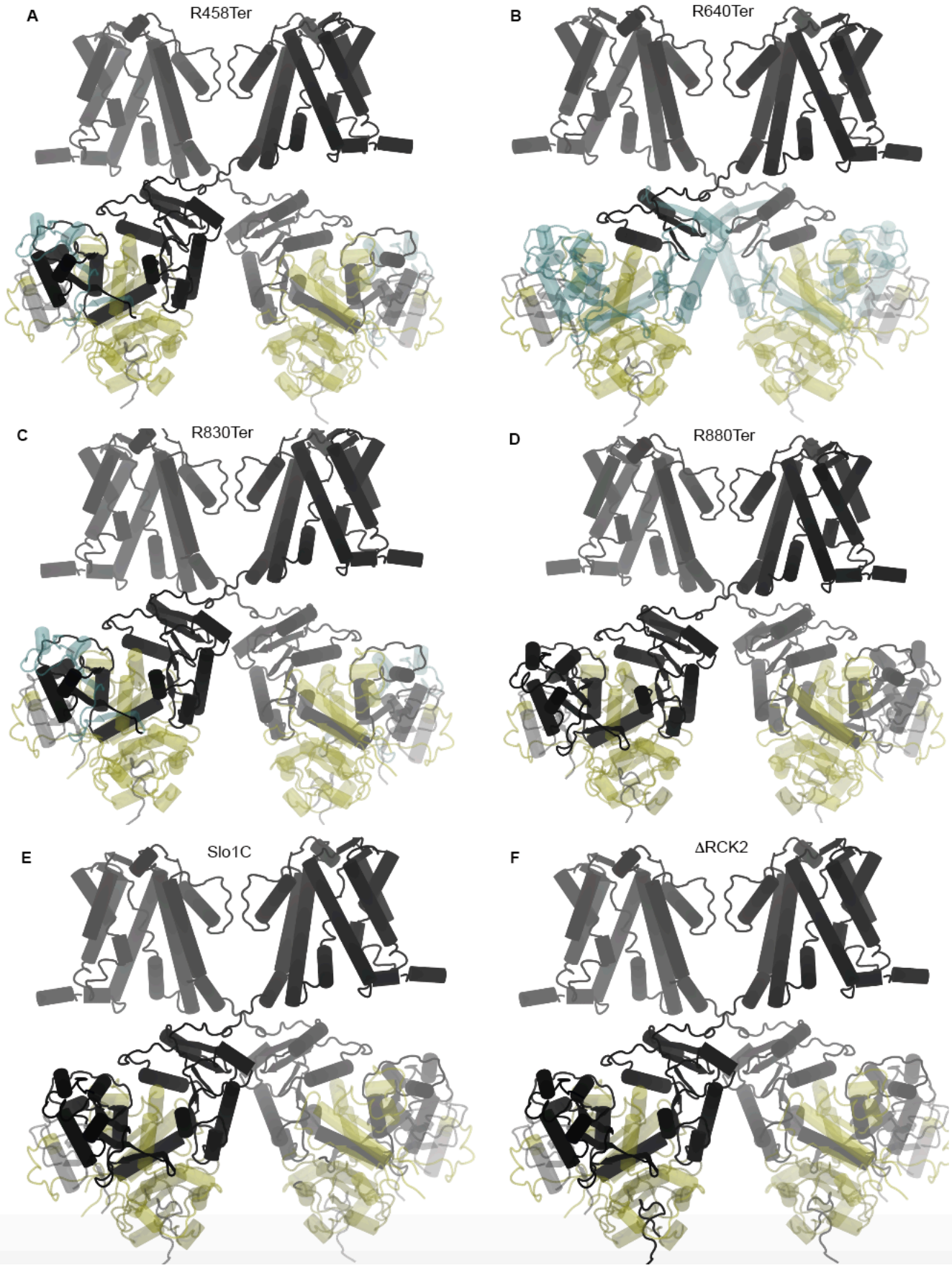

Figure 6

A

	CADD/Phred	MetaLR	Mutpred	REVEL	WSM	KMS
A172T	27.9	0.34	0.70	0.90	4.32	4.48
A314T	27.4	0.21	0.70	0.29	2.41	3.20
S351Y	27.4	0.96	0.82	0.95	5.62	5.78
G354S	29.2	0.63	0.76	0.94	5.01	5.17
G356S	29.2	0.63	0.76	0.94	5.01	5.17
G375R	29.9	0.44	0.79	0.97	4.83	5.36
C413Y	30.0	0.55	0.59	0.72	4.05	4.83
D434G	21.3	0.13	0.59	0.63	3.02	3.18
H444Q	22.6	0.28	0.61	0.55	3.08	3.47
K457E	0.01	0.01	0.01	0.01	0.64	0.75
K518N	23.4	0.09	0.47	0.14	1.44	1.60
N536H	27.4	0.37	0.64	0.67	3.63	5.13
I663V	24.6	0.79	0.58	0.67	4.22	4.39
P805L	27.3	0.39	0.00	0.62	2.69	2.85
E884K	32.0	0.43	0.41	0.56	3.18	3.71
D965V	27.6	0.31	0.34	0.44	2.49	2.65
D984N	29.4	0.41	0.38	0.37	2.55	3.08
N999S	26.0	0.81	0.36	0.71	4.07	5.57
R1097H	26.5	0.80	0.37	0.71	4.07	4.24
R1128W	29.4	0.61	0.00	0.50	2.72	2.88
N1159S	22.3	0.15	0.14	0.40	1.80	1.96

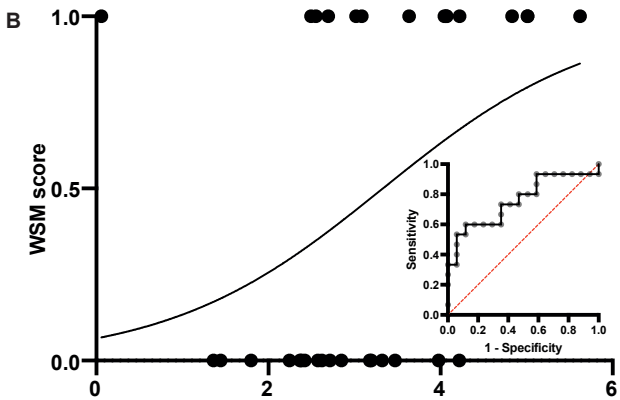

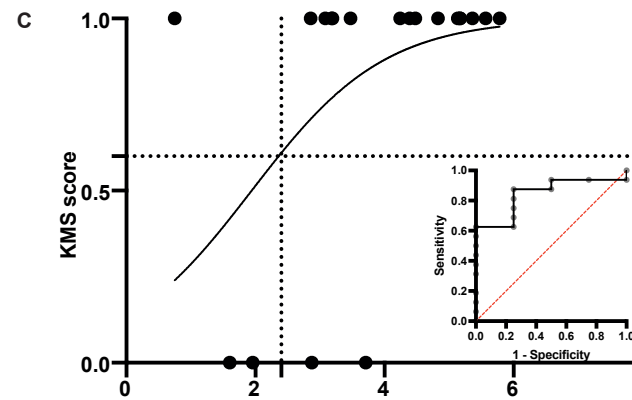

Figure 7

A

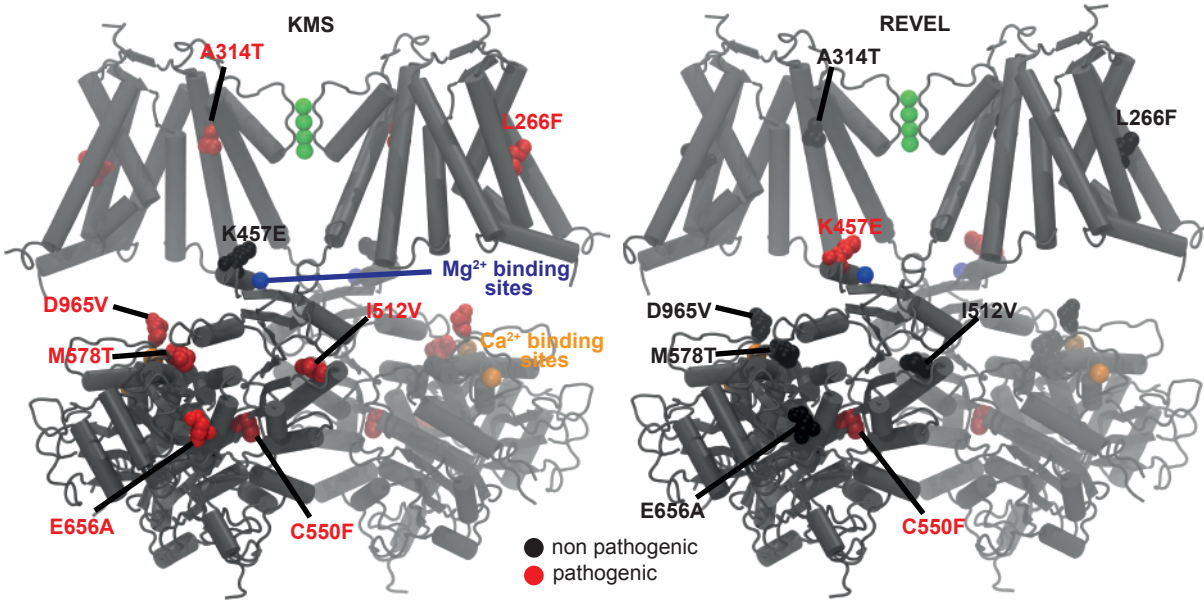

B

	KMS	REVEL
L226F	2.87	0.25
A314T	3.20	0.29
K457E	0.75	0.65
I512V	2.92	0.31
C550F	4.16	0.63
M578T	3.05	0.42
E656A	2.73	0.49
D800Y	2.58	0.58
D965V	2.65	0.44

Figure 8

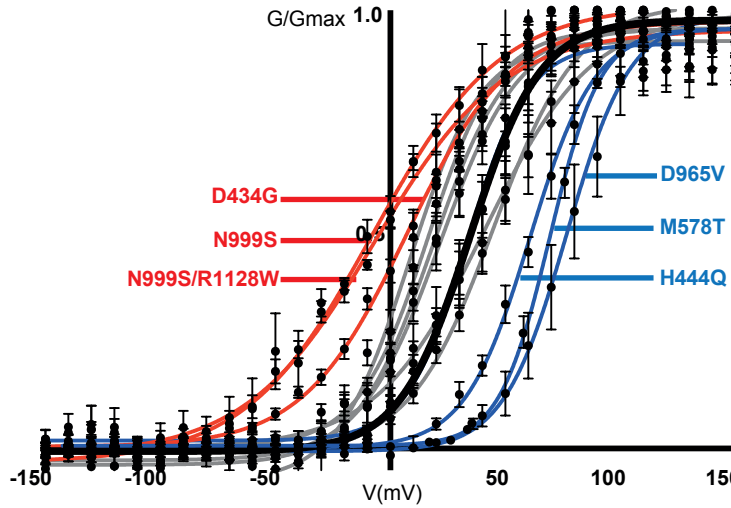
G/Gmax
1.0
0.5
D434G
N999S
N999S/R1128W
D965V
M578T
H444Q
-150
-100
-50
50
100
150
V(mV)

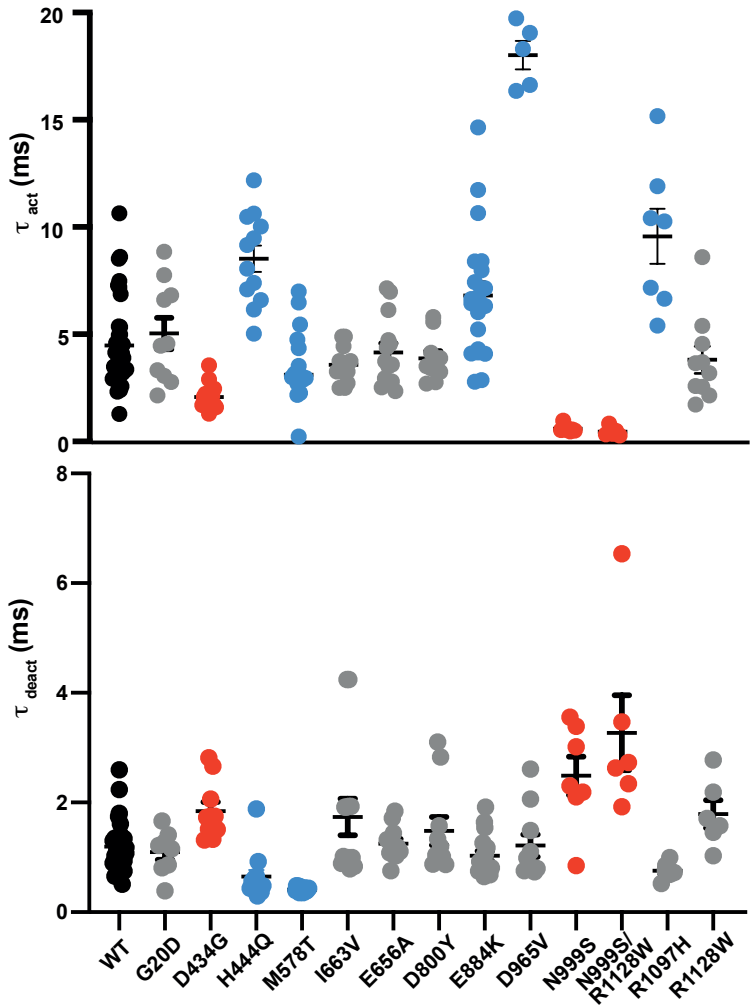
τ act (ms)
20
15
10
5
0
τ deact (ms)
8
6
4
2
0
WT
G20D
D434G
H444Q
M578T
I663V
E656A
D800Y
E884K
D965V
N999S
N999S/ R1128W
R1097H
R1128W